Ronzani, Alberto; Karimi, Bayan; Senior, Jorden; Chang, Yu Cheng; Peltonen, Joonas T.; Chen, Chii Dong; Pekola, Jukka P.

Tunable photonic heat transport in a quantum heat valve

Published in:
Nature Physics

DOI:
10.1038/s41567-018-0199-4

Published: 01/01/2018

Document Version
Peer-reviewed accepted author manuscript, also known as Final accepted manuscript or Post-print

Please cite the original version:
Ronzani, A., Karimi, B., Senior, J., Chang, Y. C., Peltonen, J. T., Chen, C. D., & Pekola, J. P. (2018). Tunable photonic heat transport in a quantum heat valve. *Nature Physics*, *14*, 991–995. https://doi.org/10.1038/s41567-018-0199-4

Tunable photonic heat transport in a quantum heat valve

Alberto Ronzani,[1,*] Bayan Karimi,[1] Jorden Senior,[1] Yu-Cheng Chang,[1,2,3]
Joonas T. Peltonen,[1] ChiiDong Chen,[1,3] and Jukka P. Pekola[1]

[1] *QTF Centre of Excellence, Department of Applied Physics, Aalto University School of Science, P.O. Box 13500, 00076 Aalto, Finland*
[2] *Department of Physics, National Taiwan University, Taipei, Taiwan, Republic of China*
[3] *Institute of Physics, Academia Sinica, Taipei, Taiwan, Republic of China*

Quantum thermodynamics is emerging both as a topic of fundamental research and as means to understand and potentially improve the performance of quantum devices [1–10]. A prominent platform for achieving the necessary manipulation of quantum states is superconducting circuit quantum electrodynamics (QED) [11]. In this platform, thermalization of a quantum system [12–15] can be achieved by interfacing the circuit QED subsystem with a thermal reservoir of appropriate Hilbert dimensionality. Here we study heat transport through an assembly consisting of a superconducting qubit [16] capacitively coupled between two nominally identical coplanar waveguide resonators, each equipped with a heat reservoir in the form of a normal-metal mesoscopic resistor termination. We report the observation of tunable photonic heat transport through the resonator-qubit-resonator assembly, showing that the reservoir-to-reservoir heat flux depends on the interplay between the qubit-resonator and the resonator-reservoir couplings, yielding qualitatively dissimilar results in different coupling regimes. Our quantum heat valve is relevant for the realisation of quantum heat engines [17] and refrigerators, that can be obtained, for example, by exploiting the time-domain dynamics and coherence of driven superconducting qubits [18, 19]. This effort would ultimately bridge the gap between the fields of quantum information and thermodynamics of mesoscopic systems.

* alberto.ronzani@aalto.fi

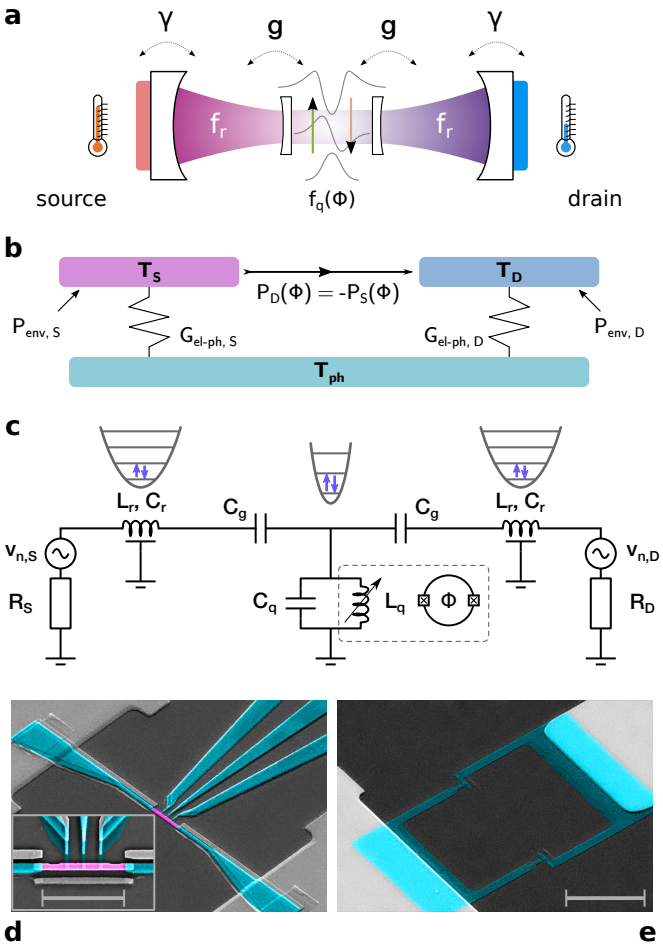

Figure 1. **Quantum Heat Valve design**. A transmon qubit having magnetic flux-tunable level spacing $f_{\rm q}(\Phi)$ is capacitively embedded between two superconducting transmission lines of identical length = 4.6 mm, each terminated by a mesoscopic normal-metal reservoir. We study the temperature of the drain reservoir $T_{\rm D}$ as a function of the temperature of the source reservoir $T_{\rm S}$ and of the ratio $r \equiv f_{\rm q}/f_{\rm r}$, where $f_{\rm r}$ is the fundamental resonant frequency of the transmission lines. **a**: Conceptual depiction of the heat valve. **b**: Thermal model. **c**: Lumped-element idealisation of the device; capacitors $C_{\rm g}$ couple the transmon to each $L_{\rm r}C_{\rm r}$ resonator. **d**: Scanning electron micrograph of a waveguide termination, including three tunnel electrodes. A copper resistor (pink, online) is in clean contact with aluminium leads (light blue, online) connecting to the patterned niobium film (light grey) on sapphire substrate (dark grey). The inset shows a magnified orthogonal view of the area spanned by the normal-metal element; the scale bar corresponds to 3 μm. **e**: Scanning electron micrograph of the SQUID element in the transmon structure; the scale bar corresponds to 10 μm.

Mesoscopic normal-metal (N) resistors are a natural candidate for the role of heat reservoirs for superconducting circuit QED experiments. Their geometry and transport properties can be adapted to provide a controllable amount of dissipation by virtue of the electron-photon interaction [20–22]. Furthermore, either clean or tunnel-type interfaces with the surrounding circuit elements enable control of impedance mismatch for a given microwave design. With their fast internal thermalization timescales [23] and slow electron-phonon relaxation [11, 24] at subkelvin temperatures, reservoirs formed of normal metal electrodes have been demonstrated as effective broadband microwave detectors [25] and sources [26]. Their thermal properties, as well as the experimental techniques required for temperature manipulation and readout, are well established and understood [27].

In this work we consider heat transmitted between two such mesoscopic reservoirs, each of which tied to the photon occupation number of a microwave resonator by the temperature-dependent Johnson-Nyquist current fluctuations of the resistor. Here, the two resonators are designed to have identical resonant frequencies $f_{\rm r}$ and they are coupled to each other via a tunable oscillator, a transmon-type qubit. This resonator-qubit-resonator assembly constitutes a Quantum Heat Valve (QHV). The thermal conductance of the QHV, conceptually depicted in Figure 1a, is expected to depend on the reservoir-resonator and resonator-qubit couplings (respectively γ, g, both normalised with respect to $f_{\rm r}$) and on the ratio r between the level spacing of the qubit and the eigenfrequency of the resonators ($f_{\rm q} \equiv r f_{\rm r}$).

For the transmon qubit, $f_{\rm q}$ depends on Φ as

$$f_{\rm q}(\Phi) = \frac{\sqrt{8E_{\rm J}(\Phi)E_{\rm C}} - E_{\rm C}}{h}\,, \tag{1}$$

where $E_{\rm C}$ and $E_{\rm J}(\Phi) = E_{\rm J0}\,|\cos(\pi\Phi/\Phi_0)|\,\sqrt{1+d^2\tan^2(\pi\Phi/\Phi_0)}$ are the charging and Josephson energies of the transmon, respectively; here, $\Phi_0 = h/2e$ is the magnetic flux quantum, and critical current asymmetry in the Superconducting QUantum Interference Device (SQUID) junctions is accounted for by the parameter d. The static dependence of the electron temperature $T_{\rm D}$ in the drain (D) reservoir is determined by the temperature of the source (S) reservoir $T_{\rm S}$ and the qubit detuning with respect to the resonators.

Figure 1b summarises the thermal model between the source and drain reservoirs. By voltage-biasing a pair of normal metal-insulator-superconductor junctions (SINIS) attached to the source reservoir one can control its temperature. At sub-gap voltages, evacuation of hot quasiparticles from the source reservoir lowers $T_{\rm S}$ below its unbiased value and above it, the biasing provides conventional Joule heating [27]. Under fixed experimental conditions, the electrons in each normal-metal reservoir are in local thermal equilibrium. In the detailed thermal balance we consider the interaction of the electron system with the environment (resulting in an effective power $P_{\rm env}$ which includes the influence of SINIS biasing where appropriate) and with the phonon bath (whose temperature $T_{\rm ph}$ is assumed to be uniform and equal to the temperature of the cryostat). The latter mechanism is modeled by the conventional normal-metal electron-phonon interaction $P_{\rm el-ph} = \Sigma\mathcal{V}(T_{\rm el}^5 - T_{\rm ph}^5)$ that for small temperature differences can be linearised with the thermal conductance $G_{\rm el-ph} = 5\Sigma\mathcal{V}T_{\rm el}^4$. Here, $\mathcal{V}$ is the volume of the normal-metal reservoir and Σ is the corresponding electron-phonon coupling constant. In the experiment, the source-to-drain heating power ($P_{\rm D} = -P_{\rm S}$ by energy conservation) is determined by the response in T_D under the assumption of the electron-phonon interaction dominating the thermal relaxation of the electrons in the drain reservoir. The lumped-element circuit representing the device is schematically illustrated in Figure 1c. Each resonator is terminated at one end by a capacitor to the transmon ($C_g \approx 8.6\,$fF) and at the other end by the normal-metal resistor to the Nb ground plane (Figure 1d). This configuration results in a quarter-wave resonator, with expected eigenfrequency $f_{\rm r} = 6.4\,$GHz and quality factor $Q_{\rm r} = Z_0/R_N \approx 20$, where $Z_0 = \pi Z_\infty/4$ is the resonance impedance and $Z_\infty = 50\,\Omega$ is the design impedance of the coplanar waveguide. Here $R_N \approx 2\,\Omega$ is the nominal resistance of the N termination; depending on the transparency of the metallic interfaces, additional dissipation can significantly decrease the effective quality factor. In our design the relaxation to the reservoir is the dominant source of losses in the resonator, so that its quality factor $Q_{\rm r} \equiv 1/\gamma$.

In modeling the system, one can consider the photonic reservoir-reservoir coupling to be relatively weak, which allows us to apply standard perturbation theory to describe it. We expect the total thermal conductance between the reservoirs to be three orders of magnitude lower than the quantum of thermal conductance of a single channel $G_{\rm Q} = (\pi k_B^2/6\hbar)T$ at temperature T [20, 28]. Here we explore two photonic weak-coupling models, each based on the formalism appropriate to the impact of reservoir-induced dissipation compared to the qubit coupling rate. We call these the quasi-Hamiltonian (QH) model for $\gamma \simeq g$, and non-Hamiltonian (NH) model applicable when $\gamma \gg g$, respectively. Conceptually, these two models showcase a different location for the Heisenberg cut (*i. e.*, the separation between the quantum subsystem and its classical environment): either at the *qubit-resonator to reservoir* boundaries or at the *qubit to resonator* interfaces, respectively. In both models, the power to each reservoir is given by

$$P_{\rm S/D} = \sum_{k,l} \rho_{kk}\, E_{kl}\, \Gamma_{k\to l,\,{\rm S/D}}\,, \tag{2}$$

where ρ is the density matrix and $E_{k,l}$, $\Gamma_{k\to l,\,{\rm S/D}}$ are the transition energy and rate for each respective reservoir, and the sum runs over all the eigenstate indices k, l.

In the absence of dissipation, a **fully-Hamiltonian (FH)** description considers that the qubit and the two resonators form a system of three coupled harmonic oscillators with level spacing $hf_{\rm q}$, $hf_{\rm r}$. This neglects both nonlinear SQUID dynamics and occupation of higher resonator harmonics, under the justification of quasi-static qubit drive and low temperatures in the two reservoirs [$\beta_{\rm S/D}hf_{\rm r} \equiv hf_{\rm r}/(k_BT_{\rm S/D}) \gg 1$], respectively. The second-quantized Hamiltonian of the hybrid system reads

$$\hat{H} = hf_{\rm r}\left[(\hat{a}_{\rm D}^\dagger\hat{a}_{\rm D} + \hat{a}_{\rm S}^\dagger\hat{a}_{\rm S}) + r\hat{b}^\dagger\hat{b} + g(\hat{b}\hat{a}_{\rm D}^\dagger + \hat{b}^\dagger\hat{a}_{\rm D} + \hat{b}\hat{a}_{\rm S}^\dagger + \hat{b}^\dagger\hat{a}_{\rm S}) + \tilde{g}(\hat{a}_{\rm D}\hat{a}_{\rm S}^\dagger + \hat{a}_{\rm D}^\dagger\hat{a}_{\rm S})\right]\,, \tag{3}$$

where $\tilde{g}$ quantifies direct resonator-to-resonator coupling. Following the low-temperature argument above, we choose the minimal four-level basis of $\{|000\rangle, |100\rangle, |010\rangle, |001\rangle\}$, where the entries in each state refer to the S-resonator, the qubit, and the D-resonator, respectively. With the addition of the parameter $a = \Delta f/f_{\rm r} \ll 1$ (quantifying possible minor asymmetry Δf between the eigenfrequencies of the two resonators), this choice of basis results in the matrix

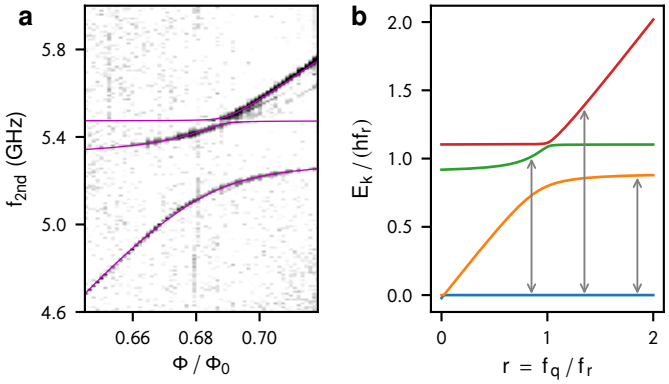

Figure 2. **Fundamental excitations of the resonator-qubit-resonator assembly. a**: Two-tone transmission spectroscopy data centered in the $f_\mathrm{r} \approx f_\mathrm{q}$ region for a sample in the fully-Hamiltonian limit. Thin lines, representing eigenvalues derived from Equation 4, are superimposed to the experimental dataset; optimal matching is obtained with parameters listed under column FH in supplementary information Table 1 with the addition of resonator asymmetry $a = 0.008$ to reproduce the secondary avoided crossing visible at $f_\mathrm{2nd} \approx 5.47\,\mathrm{GHz}$. **b**: Overview of the dominant steady-state transitions between eigenstates contributing to heat transport in the quasi-Hamiltonian limit according to Equation 5. For visual clarity, here $g = -\tilde{g} = 0.1$, $a = 0.05$.

representation

$$\hat{H} = hf_\mathrm{r} \begin{pmatrix} 0 & 0 & 0 & 0 \\ 0 & 1+a/2 & g & \tilde{g} \\ 0 & g & r & g \\ 0 & \tilde{g} & g & 1-a/2 \end{pmatrix} . \tag{4}$$

In the $a \to 0$, $r \to 0$ limit, the photon cavity modes contribute a pair of eigenstates corresponding to the symmetric and antisymmetric combinations of the eigenmodes localized in each resonator. They are in general non-degenerate due to $\tilde{g} \neq 0$, and only the symmetric combination interacts with the qubit via g. These features are evident in the dispersion of the eigenenergies shown in Figure 2b, where the dominant transitions between the levels are also indicated. To directly probe the flux-dependent spectrum of eigenstates of the QHV in the FH limit ($\gamma \ll g$), we use a design where the CPWs in the source and drain resonators are connected directly to the ground plane without resistors. In this design, a diagnostic resonator ($f_\mathrm{d} \approx 7.4\,\mathrm{GHz}$) is capacitively coupled ($C_\mathrm{d} \approx 3.4\,\mathrm{fF}$) to the top arm of the transmon island and inductively coupled to a microwave feedline. Typical two-tone spectroscopic data, obtained by standard [29] transmission readout of the diagnostic resonator is shown in Figure 2a. Inspection of the transition branches indicates that the coupling capacitance C_g induces a 216 MHz-wide avoided crossing with the symmetric resonator eigenmode, consistent with $g = 0.02$. Additionally, a small ($< 1\%$) asymmetry in resonator eigenfrequencies allows the interaction between the qubit and the antisymmetric S/D resonator eigenmode, visible as a minor avoided crossing at $f_\mathrm{2nd} \approx 5.47\,\mathrm{GHz}$. These figures set the typical power scale of the qubit-mediated heat transfer to $hf_\mathrm{r}^2 g \approx 0.4\,\mathrm{fW}$.

We now consider the effect of introducing moderate dissipation to the system via the S/D reservoirs, *i. e.*, the **quasi-Hamiltonian (QH) regime**. Equation 2 allows us to determine the power from the S-reservoir to the D-reservoir as

$$P_\mathrm{D} = \frac{2\pi h f_\mathrm{r}^2}{Q_\mathrm{r}} \sum_{k,\,l} \rho_{kk} \frac{|\langle k|\hat{a}_\mathrm{D} - \hat{a}_\mathrm{D}^\dagger|l\rangle|^2}{1 + Q_\mathrm{r}^2 \left(f_{kl}/f_\mathrm{r} - f_\mathrm{r}/f_{kl}\right)^2} \frac{(E_{kl}/hf_\mathrm{r})^2}{1 - e^{-\beta_\mathrm{D} E_{kl}}} . \tag{5}$$

Here, the steady-state balance of the transition rates $\Gamma_{k\to l}$ determines the level populations ρ_{kk}. In this model, P_D is: i) limited by the reciprocal quality factor $Q_\mathrm{r}^{-1} \equiv \gamma$; ii) non-vanishing at all values of flux even far away from the resonance; iii) affected, around $f_\mathrm{q} = f_\mathrm{r}$, by fast variation of populations, energy splitting, and matrix elements. Experimental data for a QH-type sample recorded at $T_\mathrm{ph} = 45\,\mathrm{mK}$ is presented in Figure 3a. Here, different traces, representing the estimate for the power absorbed by the drain reservoir, correspond to different thermal biases applied between the source reservoir (T_S, controlled in the $100 \to 330\,\mathrm{mK}$ range) and the drain reservoir (unbiased temperature $T_\mathrm{D} \approx 100\,\mathrm{mK}$). The traces show a sizeable amount of flux-independent power transmitted to the drain reservoir. This is particularly impressive for complete resonator-qubit detuning for applied flux corresponding to half-integer values of Φ_0. The origin of this power flow between the reservoirs lies in the role of the two mixed S/D resonator eigenmodes

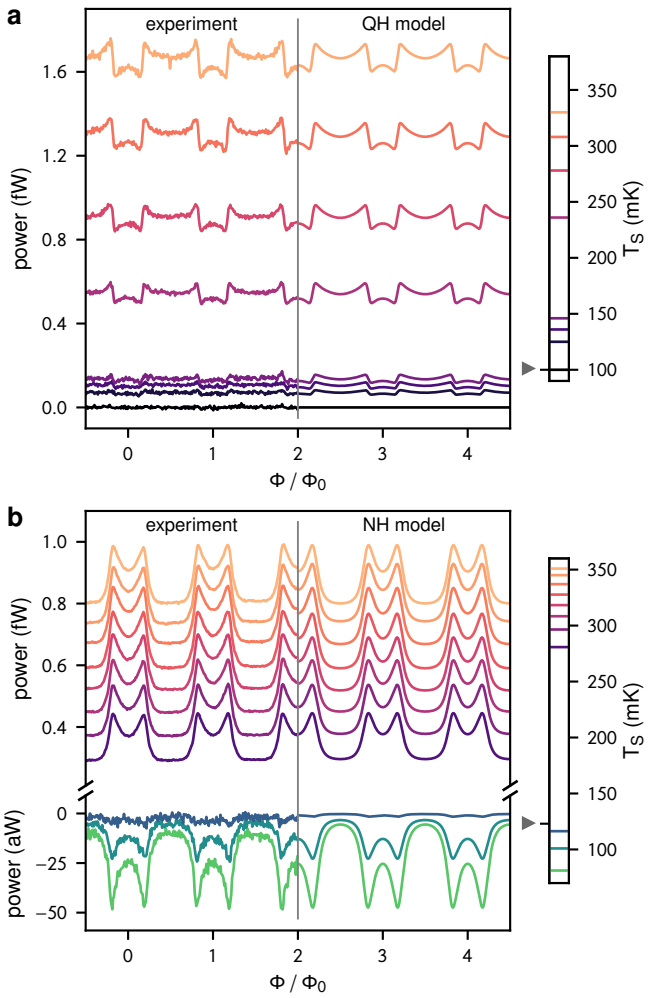

Figure 3. **Modulation of photonic heat transport.** Total heating power absorbed by the drain reservoir as a function of the applied magnetic flux Φ. Different traces correspond to the source temperature values T_S shown in the adjacent legend bar. The unbiased temperature of the drain reservoir is here marked by a triangle. In each plot, experimental data is juxtaposed to the optimal fit of the appropriate theoretical model. Panels **a**, **b** correspond to quasi-Hamiltonian (Equation 5) and non-Hamiltonian (Equation 6) regimes, respectively. Relevant modeling parameters are listed in supplemantary information Table 1. Residual reservoir-reservoir coupling, mediated by weak on-chip thermal conductance, is represented by an additional power-law contribution $P_0 = \xi[(T_\mathrm{S}/T_\mathrm{D})^n - 1]$, where $\xi = 5.14\,\mathrm{aW}$ and $n = 4.63$ are empirical parameters.

spanning the whole resonator-qubit-resonator assembly. Remarkably, approaching the $f_\mathrm{q} > f_\mathrm{r}$ condition near integer flux bias values results in an initial increase of the absorbed power, followed by a step-like decrease and a partial revival when reaching integer Φ/Φ_0 values, where $f_\mathrm{q}(\Phi)$ is maximal. The comparison with the theoretical prediction provided by Equation 5 with the nominal $Q_\mathrm{r} = 20$ value indicates that the model captures all these features quantitatively. In this case, optimal reproduction of experimental data is found, according to the estimates presented in supplementary information Table 1, with $g \approx 0.019$ and $\tilde{g} \approx -0.020$. These values compare well to the ones directly measured from the two-tone spectroscopy of the FH-type samples; notably, $g/\gamma = gQ_\mathrm{r} \approx 0.4$.

The NH model is described in Ref. [19]. The power from S-reservoir to the D-reservoir reads

$$\begin{aligned} P_\mathrm{D} = {} & \pi h g f_\mathrm{r}^2 \frac{n(\beta_\mathrm{S} h f_\mathrm{q}) - n(\beta_\mathrm{D} h f_\mathrm{q})}{[1 + Q_\mathrm{r}^2(r - 1/r)^2][\coth(\beta_\mathrm{S} h f_\mathrm{q}/2) + \coth(\beta_\mathrm{D} h f_\mathrm{q}/2)]} \\ & + \pi h \kappa f_\mathrm{r}^2 \int_0^\infty \frac{n(x\,\beta_\mathrm{S} h f_\mathrm{r}) - n(x\,\beta_\mathrm{D} h f_\mathrm{r})}{[1 + Q_\mathrm{r}^2(x - 1/x)^2]^2} x^3 \mathrm{d}x \end{aligned}, \tag{6}$$

where $n(\beta_{\mathrm{S/D}} hf) = 1/(\exp(\beta_{\mathrm{S/D}} hf) - 1)$ is the equilibrium mode population in each resonator; the second term describes direct resonator-to-resonator photon transfer, quantified by κ. Overall, P_D is: i) limited by the couplings

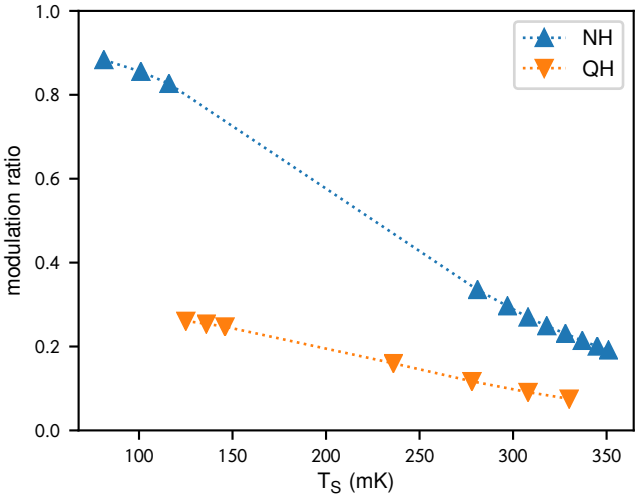

Figure 4. **Quantum Heat Valve performance.** Valve modulation ratio $(\max_\Phi P_\mathrm{D} - \min_\Phi P_\mathrm{D})/\max_\Phi |P_\mathrm{D}|$ as a function of the source temperature T_S for non-Hamiltonian and quasi-Hamiltonian regimes. Dotted lines are intended as a visual aid.

g, κ (as opposed to γ in the QH model); ii) peaking when the qubit transition frequency matches the resonator eigenfrequency, $f_\mathrm{q} = f_\mathrm{r}$; iii) inhibited when the qubit-resonator detuning exceeds the resonator linewidth $|f_\mathrm{q} - f_\mathrm{r}|/f_\mathrm{r} \gg Q_\mathrm{r}^{-1}$. The flux dependence of the power to the D-reservoir recorded at $T_\mathrm{ph} = 55\,\mathrm{mK}$ for an NH-design device is shown in Figure 3b. This dependence is consistent with the expectations based on Equation 6. Here, different traces, representing the estimate of the power absorbed by the drain reservoir, correspond to different thermal biases applied between the source reservoir (T_S, controlled in the $80 \rightarrow 360\,\mathrm{mK}$ range) and the drain reservoir (unbiased temperature $T_\mathrm{D} \approx 120\,\mathrm{mK}$). The modulation of all traces shows clear presence of two broad peaks per flux period, corresponding to the condition $f_\mathrm{q} = f_\mathrm{r}$. The shape of the flux modulation appears independent of the sign of the thermal bias. This sign reversal can be observed in the traces corresponding to the three lowest values of T_S, obtained by electron-cooling (instead of heating) of the source reservoir with an appropriate sub-gap voltage bias of a SINIS junction pair. In this figure, experimental data is juxtaposed to the best fit of Equation 6 yielding the parameter estimates listed in supplementary information Table 1, in particular $Q_\mathrm{r} = 3.15 \pm 0.14$. Such a low quality factor fully justifies the adoption of the NH model, even in the presence of a non-negligible coupling: $g/\gamma = gQ_\mathrm{r} \approx 0.05$.

In the NH case, the number of photonic excitations in each resonator is dominated by dissipative processes in the reservoirs. Under this hypothesis, the overdamping prevents the formation of the mixed S/D eigenmodes characteristic of the Hamiltonian limit. Notably, the presence of these excitations (spectroscopically probed in the FH sample, where $g/\gamma \gg 1$), is required to quantitatively reproduce via Equation 5 the heat modulation observed in the QH sample, in spite of its arguably low $g/\gamma \approx 0.4$. In the NH limit, instead, the excitation of the qubit acts as an independent flux-tunable spectral filter between the photonic populations tied to the source and drain reservoirs (Equation 6). Figure 4 presents a comparison of QH and NH samples in terms of performance as a heat valve. We see that the highest modulation ratio is obtained in the NH sample for low temperatures, where the flux-independent "background" contributions are small in comparison to the actual photonic power.

The Quantum Heat Valve presented here is a key platform dedicated to the investigation of quantum thermodynamic phenomena in hybrid mesoscopic/circuit QED systems. Planning devices including active thermal degrees of freedom requires matching resonator eigenenergies to the expected reservoir temperature. The principal heat transport bottleneck can be the resonator-qubit coupling, typically $g \lesssim 0.05$ for coplanar elements. On the other hand, a comparably strong resonator-reservoir relaxation mechanism is required for the thermalization of the relevant photonic mode population. We find that the competition between qubit-resonator and reservoir-resonator couplings affects strongly not only the power scale of the heat transport, but also the locality of its physical origin.

Methods

Fabrication protocols The devices were fabricated on $330\,\mu\mathrm{m}$ thick sapphire substrates coated with 200 nm-thick sputtered niobium film. Broader features, such as coplanar waveguides, transmon island and electrode fanout were patterned by reactive ion etching on an electron-beam lithography-defined mask. The CPW design features a $20\,\mu$m-wide centreline spaced by $10\,\mu$m with respect to the ground plane, resulting in capacitance and inductance per unit

length of 153 fF/mm and 403 pH/mm respectively. All chip layouts are available in the Supplementary Information. Nanostructures including the tunnel junction elements were realised in two steps with shadow-mask electron-beam lithography on a 1 μm-thick poly(methyl-metacrylate) / copolymer resist bilayer, followed by tilted thin film deposition in an electron-beam evaporator. In the first step, two offset depositions of 28 nm-thick Al layers (with intermediate oxidation) are performed to realise the transmon SQUID (Figure 1e) with typical per-junction tunnel resistance $R_{\mathrm{T}} \approx 7\,\mathrm{k}\Omega$ at cryogenic temperature. In the second step, the terminations of the resonators are realised by first depositing and oxidising a 15 nm-thick Al layer, followed by a 50 nm Cu layer and finally by a 85 nm-thick Al layer in clean contact with the Cu layer. The typical tunnel resistance is $R_{\mathrm{NIS}} \approx 25\,\mathrm{k}\Omega$; during the experiment, these electrodes are connected to fanout lines for the setting and readout of the electron temperature in the reservoirs over a typical timescale of tens of milliseconds. In both steps, the contact between the Nb substrate and the deposited metal is facilitated by *in situ* Ar ion plasma milling, while tunnel junctions are realised by controlled oxidation (oxygen partial pressure $\approx 10\,\mathrm{mbar}$ for 8 min). After liftoff in acetone and cleaning in isopropyl alcohol, the substrates are diced to size ($4 \times 8\,\mathrm{mm}$ for QH/NH-type and $7 \times 7\,\mathrm{mm}$ for FH-type chips) with a diamond-coated resin blade and wire-bonded to a custom made brass chip carrier for the cryogenic characterisation.

Measurements The experiment has been performed in a custom-made dilution refrigerator able to reach base temperature values $\approx 50\,\mathrm{mK}$. The bonded chip, shielded by two brass Faraday enclosures, is connected to the room-temperature breakout box with conventional cryogenic signal lines. Each line is filtered by a 1 m-long Thermocoax wire segment, resulting in an effective signal bandwidth of $0 - 10\,\mathrm{kHz}$, for low-impedance loads. Magnetic field is applied perpendicular to the sample substrate by a superconducting magnet wound on the exterior of the insert vacuum can. The latter is inserted in a high-permeability magnetic shield.

Current and voltage electrical bias are applied by programmable voltage sources and function generators with appropriate room-temperature resistor networks. Current and voltage amplification is performed by room-temperature low-noise amplifiers (FEMTO Messtechnik GmbH, models DLPCA-200 and DLPVA-100). In order to minimise the impact of signal pickup and low-frequency drifts of the differential voltage amplifier output in the SINIS thermometer readout, temperature signals are derived from the first harmonic recorded by a lock-in amplifier synchronised to the square-wave modulation (42 Hz) of the voltage bias of the source reservoir SINIS circuit. The noise-equivalent spectral density obtained in this differential readout scheme is $0.1\,\mathrm{mK}/\sqrt{\mathrm{Hz}}$, corresponding to typical uncertainty $\delta T \approx 40\,\mu\mathrm{K}$ (r.m.s.) in the temperature estimates (effective integration bandwidth = 0.14 Hz for the lock-in measurement). Quantitative estimates of the bias-dependent power absorbed by the drain reservoir are obtained assuming that the electron-phonon interaction dominates the thermal relaxation, yielding

$$P_{\mathrm{D}} \approx \Sigma \mathcal{V} T_{\mathrm{D}}^4 \Delta T_{\mathrm{D}}\,, \tag{7}$$

where ΔT_{D} is the peak-peak amplitude of the signal recorded by the drain thermometer.

ACKNOWLEDGEMENTS

This work was funded through Academy of Finland grants 297240, 312057 and 303677 and from the European Union's Horizon 2020 research and innovation programme under the European Research Council (ERC) programme and Marie Sklodowska-Curie actions (grant agreements 742559 and 766025). This work was supported by Centre for Quantum Engineering (CQE) at Aalto University. We acknowledge the facilities and technical support of Otaniemi research infrastructure for Micro and Nanotechnologies (OtaNano), and VTT technical research center for sputtered Nb films. We acknowledge M. Meschke for technical help and O-P. Saira for useful discussions in the initial stages of this work. We thank D. Golubev and Y. Galperin for helpful discussions.

AUTHOR CONTRIBUTIONS

The experiment was conceived by J.P. and B.K., with contributions from CD.C. A.R. performed the experiment. A.R., J.S. and Y-C.C. designed and fabricated the samples. Data analysis was performed by A.R. based on theoretical models conceived and solved by J.P. and B.K. Y.-C.C. performed the spectroscopy measurements. J.T.P. provided technical support in fabrication, low-temperature setups and measurements. All authors have been involved in the discussion of scientific results and implications of this work. The manuscript was written by A.R. with contributions from J.P., B.K., and J.S.

SUPPLEMENTARY INFORMATION

Chip design

A rendered image of the quantum heat valve is shown in Fig. 5.

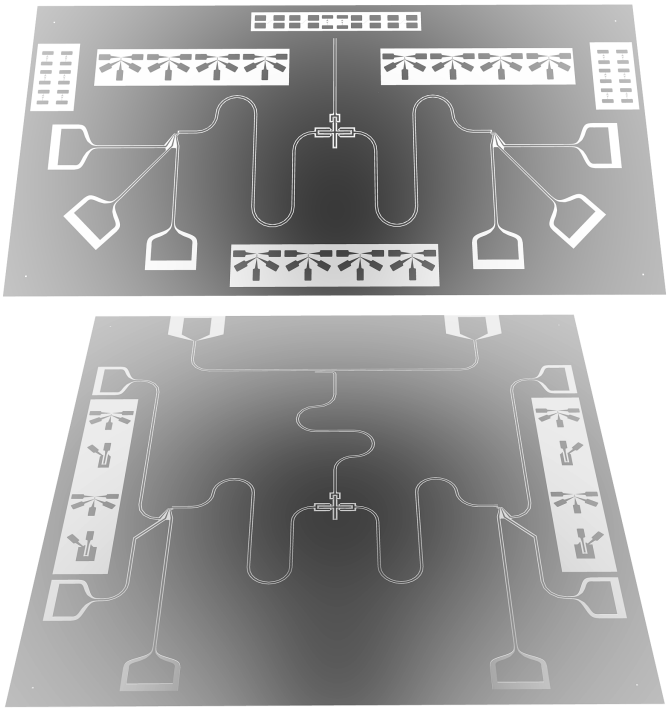

Figure 5. Renders of the coplanar microwave structure of a quantum heat valve device. The dark areas represent metallic Nb film after the etching step. The additional structures at the periphery are fabricated for diagnostic purposes and are not part of the actual device. The **top image** refers to samples of type QH/NH in the main text (4x8 mm). Here the cross-shaped transmon element is coupled to identical quarter-wave resonators (left and right), each of which is terminated by a normal-metal Cu shunt to the common ground plane. The three contact pads near the bottom corners of the device are connected to NIS probes on the normal-metal terminations of the resonators. The **bottom image** refers instead to FH-type samples (7x7 mm). In this design, each quarter-wave resonator is directly connected to the ground plane, and a 7.4 GHz diagnostic resonator couples the top terminal of the transmon structure to a feedline for spectroscopy characterization via transmission microwave readout. In this design, the fanout for the probe electrodes is still patterned in the Nb film, but no actual NIS elements are present near the quarter-wave shunt terminations.

Device parameters

A summary of device parameters is presented in Tab. I.

	design	**FH**	**QH**	**NH**
f_r (GHz)	6.4	5.39	5.30 ± 0.04	5.61 ± 0.15
Q_r	20	N/A	20	3.15 ± 0.14
$g \times 10^2$	2.0	2.0	1.93 ± 0.02	1.56 ± 0.06
$\tilde{g} \times 10^2$	N/A	-1.5	-2.01 ± 0.05	N/A
$\kappa \times 10^2$	N/A	N/A	N/A	0.21 ± 0.05
E_C/h (GHz)	0.2	0.15	0.15	0.15
E_J0/h (GHz)	45	45.0	28.8 ± 0.3	35.7 ± 1.1
d	N/A	N/A	0.57 ± 0.01	0.08 ± 0.59

Table I. Summary of parameter estimates and measurements. Values quoted with uncertainty are parameter estimates obtained by fitting Equations 5 and 6 (main article text) to experimental data recorded for samples QH and NH, respectively. Values quoted without uncertainty, either by design or measured on FH-type samples, have been used as constraints in modeling samples QH, NH.

The Hamiltonian

In the general case, we assume the qubit to be fully harmonic and capacitively coupled (g) to two resonators, also modelled as harmonic oscillators. The two resonators have eigen-frequency and quality factor f_r, Q_r, respectively, while the energy splitting of the harmonic potential of the transmon is hf_q. Since the non-Hamiltonian model for $gQ_\mathrm{r} \ll 1$ is described elsewhere [30, 31], we focus here only on the quasi-Hamiltonian applicable when $gQ_\mathrm{r} \gtrsim 1$.

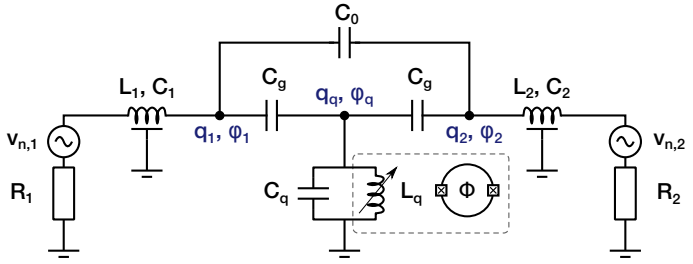

Figure 6. Lumped-element approximation of the quantum heat valve. The notations for phases φ_i, charges q_i, capacitances C_i, inductances L_i, and resistances R_i in the text can be read in this figure.

Figure 6 shows a lumped-element approximation of the system. In particular, to include an example of a direct resonator-resonator photon transfer mechanism, we introduce the shunting capacitor C_0. The Lagrangian of the circuit consisting of parallel LC resonators in this case reads then

$$\mathfrak{L}(\varphi_1,\dot{\varphi}_1,\varphi_\mathrm{q},\dot{\varphi}_\mathrm{q},\varphi_2,\dot{\varphi}_2) = \frac{1}{2}\big(C_1\dot{\varphi}_1^2 + C_\mathrm{g}(\dot{\varphi}_\mathrm{q}-\dot{\varphi}_1)^2 + C_\mathrm{q}\dot{\varphi}_\mathrm{q}^2 + C_\mathrm{g}(\dot{\varphi}_\mathrm{q}-\dot{\varphi}_2)^2 + C_0(\dot{\varphi}_1-\dot{\varphi}_2)^2 + C_2\dot{\varphi}_2^2\big) - \frac{1}{2}\big(\frac{\varphi_1^2}{L_1} + \frac{\varphi_\mathrm{q}^2}{L_\mathrm{q}} + \frac{\varphi_2^2}{L_2}\big). \quad (8)$$

From the Lagrangian we can obtain the conjugate momenta of node fluxes by the Legendre transformation $q_\mathrm{n} = \frac{\partial \mathfrak{L}}{\partial \dot{\varphi}_\mathrm{n}}$, yielding:

$$H = \big(\frac{q_1^2}{2C_{1,\mathrm{eff}}} + \frac{\varphi_1^2}{2L_1}\big) + \big(\frac{q_\mathrm{q}^2}{2C_{\mathrm{q,eff}}} + \frac{\varphi_\mathrm{q}^2}{2L_\mathrm{q}}\big) + \big(\frac{q_2^2}{2C_{2,\mathrm{eff}}} + \frac{\varphi_2^2}{2L_2}\big) + C_{1\mathrm{q}}^{-1} q_\mathrm{q} q_1 + C_{2\mathrm{q}}^{-1} q_\mathrm{q} q_2 + C_{12}^{-1} q_1 q_2\,. \quad (9)$$

Applying symmetry considerations for this system, namely $C_1 = C_2 \equiv C_\mathrm{r}$ and $L_1 = L_2 \equiv L_\mathrm{r}$, and for $C_\mathrm{g} \ll C_\mathrm{r}, C_\mathrm{q}$ (considering up to linear in C_g terms only)

$$\begin{aligned}
C_{1,\mathrm{eff}}^{-1} &= C_{2,\mathrm{eff}}^{-1} = \frac{C_0 + C_\mathrm{r}}{2C_0C_\mathrm{r} + C_\mathrm{r}^2} - C_\mathrm{g}\frac{2C_0^2 + 2C_0C_\mathrm{r} + C_\mathrm{r}^2}{(2C_0C_\mathrm{r} + C_\mathrm{r}^2)^2} \\
C_{\mathrm{q,eff}}^{-1} &= \frac{1}{C_\mathrm{q}}\big(1 - \frac{2C_\mathrm{g}}{C_\mathrm{q}}\big) \\
C_{12}^{-1} &= \frac{C_0}{2C_0C_\mathrm{r} + C_\mathrm{r}^2} - \frac{2C_0(C_0 + C_\mathrm{r})C_g}{C_\mathrm{r}^2(2C_0 + C_\mathrm{r})^2} \\
C_\mathrm{c}^{-1} &\equiv C_{1\mathrm{q}}^{-1} = C_{2\mathrm{q}}^{-1} = \frac{C_\mathrm{g}}{C_\mathrm{q}C_\mathrm{r}}.
\end{aligned} \quad (10)$$

The Hamiltonian based on the charge operators $\hat{q}_\mathrm{i} = -i\sqrt{\frac{\hbar}{2Z_0}}(\hat{a}_\mathrm{i} - \hat{a}_\mathrm{i}^\dagger)$ and $\hat{q}_\mathrm{q} = -i\sqrt{\frac{\hbar}{2Z_0}}(\hat{b} - \hat{b}^\dagger)$ is given by

$$(hf_\mathrm{r})^{-1}\hat{H} = \hat{a}_1^\dagger\hat{a}_1 + \hat{a}_2^\dagger\hat{a}_2 + r\hat{b}^\dagger\hat{b} + g(\hat{b}\hat{a}_1^\dagger + \hat{b}^\dagger\hat{a}_1 + \hat{b}\hat{a}_2^\dagger + \hat{b}^\dagger\hat{a}_2) + \tilde{g}(\hat{a}_1\hat{a}_2^\dagger + \hat{a}_1^\dagger\hat{a}_2), \tag{11}$$

where $g = (4\pi Z_0 C_\mathrm{c} f_\mathrm{r})^{-1}$, $\tilde{g} = (4\pi Z_0 C_{12} f_\mathrm{r})^{-1}$, $r = f_\mathrm{q}/f_\mathrm{r}$, and $Z_0 = \sqrt{L_\mathrm{r}/C_\mathrm{r}}$. Here $\hat{a_\mathrm{i}}^\dagger, \hat{b}^\dagger$ and $\hat{a}_\mathrm{i}, \hat{b}$ are the creation and annihilation operators, respectively. In the product basis $\{|000\rangle, |100\rangle, |010\rangle, |001\rangle\}$ where the first entry refers to the left resonator, second one to the qubit, and the last one to the right resonator we have then the result

$$H = hf_r \begin{pmatrix} 0 & 0 & 0 & 0 \\ 0 & 1 & g & \tilde{g} \\ 0 & g & r & g \\ 0 & \tilde{g} & g & 1 \end{pmatrix}, \tag{12}$$

The dimensionless eigenenergies $\lambda_k = E_k/(hf_\mathrm{r})$ of this Hamiltonian are

$$\begin{aligned} \lambda_1 &= 0 \\ \lambda_2 &= 1 - \tilde{g} \\ \lambda_3 &= \frac{1}{2}[1 + \tilde{g} + r - \sqrt{1 + 2\tilde{g} + \tilde{g}^2 + 8g^2 - 2r - 2\tilde{g}r + r^2}] \\ \lambda_4 &= \frac{1}{2}[1 + \tilde{g} + r + \sqrt{1 + 2\tilde{g} + \tilde{g}^2 + 8g^2 - 2r - 2\tilde{g}r + r^2}] \end{aligned} \tag{13}$$

These energy levels, and the allowed transition rates between them are shown in Fig. 2b of the main text.

Coupling to thermal noise: transition rates and power

Consider first the resonator as a series LC circuit, whose impedance is

$$Z = iZ_0(f/f_\mathrm{r} - f_\mathrm{r}/f). \tag{14}$$

With series resistance R, the quality factor of the resonance is $Q_\mathrm{r} = Z_0/R$.

In reality, the resonator is a $\lambda/4$ transmission line terminated by an open circuit (by a small gate capacitance). Its impedance is given by

$$Z = \frac{e^{2ikl} - \chi}{e^{2ikl} + \chi} Z_\infty, \tag{15}$$

where the reflection coefficient $\chi = (Z_\infty - Z_\mathrm{L})/(Z_\infty + Z_\mathrm{L}) \to -1$, when the load impedance $Z_\mathrm{L} \to \infty$. Here Z_∞ equals $\sqrt{L_0/C_0}$ with L_0, C_0 the inductance and capacitance per unit length of the line. Near the resonance, i.e. for $k = k_0 + \delta k$ values near $k_0 l = \pi/2$, we may expand Z with the result

$$Z \approx i\frac{\pi}{4} Z_\infty (f/f_\mathrm{r} - f_\mathrm{r}/f), \tag{16}$$

where $k_0 = \omega_0\sqrt{L_0 C_0}$. Then with $Q_\mathrm{r} = Z_0/R$, where $Z_0 = \frac{\pi}{4}Z_\infty$, we obtain identical results with the lumped series resonator above. In both cases, the fluctuating voltage seen by the harmonic oscillator is normalized to

$$v(t) = \frac{R}{R + iZ_0(f/f_\mathrm{r} - f_\mathrm{r}/f)} v_\mathrm{n}(t), \tag{17}$$

where $v_\mathrm{n}(t)$ is the noise of the resistor alone with spectrum

$$S_{v_n}(f) = \frac{2Rhf}{1 - e^{-\beta hf}}. \tag{18}$$

Then

$$S_v(f) = \frac{1}{1 + Q_\mathrm{r}^2(f/f_\mathrm{r} - f_\mathrm{r}/f)^2} \frac{2Rhf}{1 - e^{-\beta hf}}. \tag{19}$$

We obtain the transition rates induced by thermal bath B between eigenstates k and l by the golden rule expression

$$\Gamma_{k\to l,\mathrm{B}} = \frac{1}{\hbar^2}|\langle k|\hat{q}_\mathrm{B}|l\rangle|^2 S_{v,\mathrm{B}}(f_{kl}). \tag{20}$$

Here $S_{v,\mathrm{B}}$ is the noise on the resonator coupled to bath B.

If the energy separations between the eigenenergies are given by $E_{kl} = hf_\mathrm{r}(\lambda_k - \lambda_l) \equiv hf_{kl}$, we then have

$$\Gamma_{k\to l,\mathrm{B}} = \frac{2\pi}{Q_\mathrm{B}} \frac{|\langle k|\hat{a}_\mathrm{B} - \hat{a}_\mathrm{B}^\dagger|l\rangle|^2}{1 + Q_\mathrm{B}^2(\frac{f_{kl}}{f_\mathrm{r}} - \frac{f_\mathrm{r}}{f_{kl}})^2} \frac{f_{kl}}{1 - e^{-\beta_\mathrm{B} h f_{kl}}}, \tag{21}$$

where Q_B is the quality factor of the resonator attached to bath B at inverse temperature β_B. Here the squared matrix elements are given by

$$\begin{aligned}
&|\langle 1|\hat{a}_\mathrm{B} - \hat{a}_\mathrm{B}^\dagger|2\rangle|^2 = |\langle 2|\hat{a}_\mathrm{B} - \hat{a}_\mathrm{B}^\dagger|1\rangle|^2 = 1/2 \\
&|\langle 1|\hat{a}_\mathrm{B} - \hat{a}_\mathrm{B}^\dagger|3\rangle|^2 = |\langle 3|\hat{a}_\mathrm{B} - \hat{a}_\mathrm{B}^\dagger|1\rangle|^2 = \frac{1}{4}(1 + \frac{r-1-\tilde{g}}{\sqrt{(r-1-\tilde{g})^2 + 8g^2}}) \\
&|\langle 1|\hat{a}_\mathrm{B} - \hat{a}_\mathrm{B}^\dagger|4\rangle|^2 = |\langle 4|\hat{a}_\mathrm{B} - \hat{a}_\mathrm{B}^\dagger|1\rangle|^2 = 1/2 - |\langle 1|\hat{a}_\mathrm{B} - \hat{a}_\mathrm{B}^\dagger|3\rangle|^2 = \frac{1}{4}(1 - \frac{r-1-\tilde{g}}{\sqrt{(r-1-\tilde{g})^2 + 8g^2}}).
\end{aligned} \tag{22}$$

Other elements vanish.

Based on the allowed transitions presented in Fig. 2b, the diagonal elements of the density matrix under non-driven conditions are given by

$$\begin{aligned}
\dot{\rho}_{11} &= -(\Gamma_{1\to2} + \Gamma_{1\to3} + \Gamma_{1\to4})\rho_{11} + \Gamma_{2\to1}\rho_{22} + \Gamma_{3\to1}\rho_{33} + \Gamma_{4\to1}\rho_{44} \\
\dot{\rho}_{22} &= -\Gamma_{2\to1}\rho_{22} + \Gamma_{1\to2}\rho_{11} \\
\dot{\rho}_{33} &= -\Gamma_{3\to1}\rho_{33} + \Gamma_{1\to3}\rho_{11} \\
\dot{\rho}_{44} &= -\Gamma_{4\to1}\rho_{44} + \Gamma_{1\to4}\rho_{11},
\end{aligned} \tag{23}$$

where $\Gamma_{k\to l} = \Gamma_{k\to l,\mathrm{S}} + \Gamma_{k\to l,\mathrm{D}}$. We apply steady state conditions as $\dot{\rho} = 0$. The power to bath B then reads

$$P_\mathrm{B} = \frac{2\pi h f_\mathrm{r}^2}{Q_\mathrm{B}} \sum_{k,l} \rho_{kk} \frac{|\langle k|\hat{a}_\mathrm{B} - \hat{a}_\mathrm{B}^\dagger|l\rangle|^2}{1 + Q_\mathrm{B}^2(\frac{f_{kl}}{f_\mathrm{r}} - \frac{f_\mathrm{r}}{f_{kl}})^2} \frac{(f_{kl}/f_\mathrm{r})^2}{1 - e^{-\beta_\mathrm{B} h f_{kl}}}\,. \tag{24}$$

[1] Vinjanampathy, S. & Anders, J. Quantum thermodynamics. Contemp. Phys. **57**, 545-579 (2016).
[2] Goold, J. & Huber, M. & Riera, A. & del Rio, L. & Skrzypczyk, P. The role of quantum information in thermodynamics—a topical review. J. Phys. A: Math. Theor. **49**, 143001 (2016).
[3] Martínez-Pérez, M. J. & Giazotto, F. The Josephson heat interferometer, Nature **492**, 401-405 (2012).
[4] Pekola, J. P. Towards Quantum Thermodynamics in electronic circuits. Nat. Phys. **11**, 118-123 (2015).
[5] Jezouin, S. & Parmentier, F. D. & Anthore, A. & Gennser U. & Cavanna, A. & Jin, Y. & Pierre, F. Quantum limit of heat flow across a single electronic channel. Science **342**, 601-604 (2013).
[6] Schwab, K. & Henriksen, E. & Worlock, J. & Roukes, M. Measurement of the quantum of thermal conductance. Nature **404**, 974-977 (2000).
[7] Banerjee, M. & Heiblum, M. & Rosenblatt, A. & Oreg, Y. & Feldman, D. E. & Stern, A. & Umansky, V. Observed quantization of anyonic heat flow. Nature **545**, 75-79 (2017).
[8] Sivre, E. & Anthore, A. & Parmentier, F. D. & Cavanna, A. & Gennser, U. & Ouerghi, A. & Jin, Y. & Pierre, F. Heat Coulomb blockade of one ballistic channel. Nat. Phys. **14**, 145-148 (2018).
[9] Cottet, N. & Jezouin, S. & Bretheau, L. & Campagne-Ibarcq, P. & Ficheux, Q. & Anders, J. & Auffèves, A. & Azouit, R. & Rouchon, P. & Huard, B. Observing a quantum Maxwell demon at work. Proc. Nat. Acad. Sci. **114**, 7561-7564 (2017).
[10] Partanen, M. & Tan, K. Y. & Masuda, S. & Govenius, J. & Lake, R. E. & Jenei, M. & Grönberg, L. & Hassel, J. & Simbierowicz, S. & Vesterinen, V. & Tuorila, J. & Ala-Nissila, T. & Möttönen, M. Flux-tunable heat sink for quantum electric circuits. Sci. Rep. **8** 6325 (2018).
[11] Wallraff, A. & Schuster, D. I. & Blais, A. & Frunzio, L. & Huang, R. -S. & Majer, J. & Kumar, S. & Girvin, S. M. & Schoelkopf, R. J. Strong coupling of a single photon to a superconducting qubit using circuit quantum electrodynamics. Nature **431**, 162-167 (2004).
[12] Neill, C. & Roushan, P. & Fang, M. & Chen, Y. & Kolodrubetz, M. & Chen, Z. & Megrant, A. & Barends, R. & Campbell, B. & Chiaro, B. & Dunsworth, A. & Jeffrey, E. & Kelly, J. & Mutus, J. & O'Malley, P.J.J. & Quintana, C. & Sank, D. & Vainsencher, A. & Wenner, J. & White, T.C. & Polkovnikov, A. & Martinis, J.M. Ergodic dynamics and thermalization in an isolated quantum system. Nat. Phys. **12**, 1037-1041 (2016).
[13] Srednicki, M. Chaos and quantum thermalization. Phys. Rev. E **50**, 888 (1994).
[14] Kaufman, A. M. & Tai, M. E. & Lukin, A. & Rispoli, M. & Schittko, R. & Preiss, P. M. & Greiner, M. Quantum thermalization through entanglement in an isolated many-body system. Science **353**, 794-800 (2016).
[15] Reimann, P. Eigenstate thermalization: Deutsch's approach and beyond. New J. Phys. **17**, 055025 (2015).
[16] Koch, J. & Yu, T. M. & Gambetta, J. & Houck, A. A. & Schuster, D. I. & Majer, J. & Blais, A. & Devoret, M. H. & Girvin, S. M. & Schoelkopf, R. J. Charge-insensitive qubit design derived from the Cooper pair box. Phys. Rev. A **76**, 042319 (2007).
[17] Roßnagel, J. & Dawkins, S. T. & Tolazzi, K. N. & Abah, O. & Lutz, E. & Schmidt-Kaler, F. & Singer, K. A sigle atom heat engine. Science **352**, 325-329 (2016).
[18] Kosloff, R. & Levy, A. Quantum heat engines and refrigerators: continuous devices. Annual Rev. Phys. Chem. **65**, 365-393 (2014).
[19] Karimi, B., & Pekola, J. P. Otto refrigerator based on a superconducting qubit: Classical and quantum performance. Phys. Rev. B **94**, 184503 (2016).
[20] Schmidt, D. R. & Schoelkopf, R. J. & Cleland, A. N. Photon-mediated thermal relaxation of electrons in nanostructures. Phys. Rev. Lett. **93**, 045901 (2004).
[21] Meschke, M. & Guichard, W. & Pekola, J. P. Single-mode heat conduction by photons. Nature **444**, 187-190 (2006).
[22] Partanen, M. & Tan, K. Y. & Govenius, J. & Lake, R. E. & Mäkelä, M. K. & Tanttu, T. & Möttönen, M. Quantum-limited heat conduction over macroscopic distances. Nat. Phys. **12**, 460-464 (2016).
[23] Pothier, H. & Gueron, S. & Birge, N. O. & Esteve, D. & Devoret, M. H. Energy distribution function of quasiparticles in mesoscopic wires. Phys. Rev. Lett. **79**, 3490 (1997).
[24] Gasparinetti, S. & Viisanen, K. L. & Saira, O.-P. & Faivre, T. & Arzeo, M. & Meschke, M. & Pekola, J. P. Fast electron thermometry towards ultra-sensitive calorimetric detection. Phys. Rev. Appl. **3**, 014007 (2015).
[25] Govenius, J. & Lake, R. E. & Tan, K. Y. & Pietilä, V. & Julin, J. K. & Maasilta, I. J. & Virtanen, P., & Möttönen, M. Microwave nanobolometer based on proximity Josephson junctions. Phys. Rev. B **90**, 064505 (2014).
[26] Tan, K. Y. & Partanen, M. & Lake, R. E. & Govenius, J. & Masuda, S. & Möttönen, M. Quantum-circuit refrigerator. Nat. Comm. **8**, 15189 (2017).
[27] Giazotto, F. & Heikkilä, T. T. & Luukanen, A. & Savin, A. M. & Pekola, J. P. Opportunities for mesoscopics in thermometry and refrigeration: Physics and applications. Rev. Mod. Phys **78**(1) 217-274 (2006).
[28] Pendry, J. B. Quantum limits to the flow of information and entropy. J. Phys. A: Math. Gen. **16**, 2161 (1983).
[29] Bianchetti, A. R. Control and readout of a superconducting artificial atom. Doctoral Thesis, ETH Zurich (2010).
[30] B. Karimi, J. P. Pekola, Otto refrigerator based on a superconducting qubit: Classical and quantum performance, Phys. Rev. B **94**, 184503 (2016).
[31] B. Karimi, J. P. Pekola, M. Campisi, and R. Fazio, Coupled qubits as a quantum heat switch, Quantum Sci. Technol. **2**, 044007 (2017).